Journal of Materials Chemistry A

PAPER

View Article Online
View Journal | View Issue

Cite this: J. Mater. Chem. A, 2018, 6, 6356

Self-templating synthesis of silicon nanorods from natural sepiolite for high-performance lithium-ion battery anodes†

Qingze Chen, [ab] Runliang Zhu, *[a] Shaohong Liu,[c] Dingcai Wu, [c] Haoyang Fu,[ab] Jianxi Zhu[a] and Hongping He[ab]

Received 18th January 2018
Accepted 6th March 2018

DOI: 10.1039/c8ta00587g

rsc.li/materials-a

Nanostructured silicon is an attractive anode material for next-generation lithium-ion batteries, but its commercialization remains a challenge owing to the energy-intensive, costly, and complex preparation of nanostructured silicon. Herein, one-dimensional (1D) silicon nanorods (SNRs) have been synthesized from natural sepiolite by a simple self-templating synthesis method. The intrinsic crystal structure and chemical composition of sepiolite allow for the maintenance of 1D structures during magnesiothermic reduction without any additional templates and heat scavengers. The as-prepared SNRs showed a large specific surface area (~122 m^2 g^{-1}) and hierarchical porous structure (*i.e.*, macro- and meso-pores). As anodes for lithium-ion batteries, SNRs exhibited a high reversible capacity of 1350 mA h g^{-1} at 1.0 A g^{-1} after 100 cycles, and 816 mA h g^{-1} at 5.0 A g^{-1} after 500 cycles (with a capacity retention of 98%). With a low-cost precursor and facile approach, this strategy for synthesizing 1D nanostructured Si would be promising in practical production of high-performance anode materials for lithium-ion batteries.

Introduction

Lithium-ion batteries (LIBs) with high power and high energy-density are being rapidly developed nowadays to meet the ever-increasing demands of hybrid electric vehicles, portable electronic devices, and smart electricity storage units.[1–4] Exploring high-performance electrode materials is the key to fabricating next-generation LIBs.[5–7] Silicon (Si) is identified as the most promising candidate to supersede the traditional graphite-based anode in commercial LIBs, owing to its high specific capacity (~3579 mA h g^{-1} based on the $Li_{15}Si_4$ alloy) and low discharge potential (<0.4 V *vs.* Li/Li^+).[8–10] However, the insufficient transport properties and huge volume change of Si anodes during repeated lithium insertion/extraction result in serious capacity decay, which hinder the practical application of Si anodes in LIBs.[11,12]

To address this problem, various Si nanostructures, including nanoparticles,[13,14] nanowires,[15,16] nanosheets,[17,18] and porous nanostructures,[19,20] have been designed to improve the structural and cycling stability of Si anodes. Due to the robust charge transport along the axis and flexible nature, one-dimensional (1D) nanostructured Si is considered as an attractive anode material for LIBs.[21,22] Furthermore, 1D nanostructures offer the advantage of allowing the volume expansion radially to minimize the cracking tendency, and the small axial dimension could facilitate the lithium ion diffusion.[11] As a result, 1D nanostructured Si exhibited good rate capability and long cycling stability.

A variety of preparation methods have been established accompanying the rising demands of 1D Si nanomaterials, such as electrochemical/electroless etching of Si wafers[23–26] and chemical vapor deposition (CVD) of gaseous Si precursors.[27–29] These conventional methods are able to produce 1D nanostructured Si with high-quality and a controlled morphology, but lack the potential of mass production due to the expensive precursors, harsh reaction conditions, and low yield. Electrospinning of silica followed by magnesiothermic reduction is another representative approach.[30–32] However, the electrospinning process is usually based on a template-assisted synthesis method. The introduction and removal of the template (*e.g.*, carbon nanofibers and organic surfactants) make this process very sophisticated,[30–32] further impeding the commercialization of 1D Si. Therefore, a low-cost, large-scale, and environment-friendly strategy for synthesizing 1D nanostructured Si is highly necessary.

In fact, the magic of nature has already created many kinds of 1D Si-containing materials, such as aciform wollastonite and fibrous sepiolite,[33–35] which inspired us to directly use these natural precursors to synthesize 1D Si. Herein, for the first time,

[a]CAS Key Laboratory of Mineralogy and Metallogeny, Guangdong Provincial Key Laboratory of Mineral Physics and Materials, Guangzhou Institute of Geochemistry, Chinese Academy of Sciences, Guangzhou 510640, China. E-mail: zhurl@gig.ac.cn

[b]University of Chinese Academy of Sciences, Beijing 100049, China

[c]Materials Science Institute, PCFM Lab and GDHPRC Lab, School of Chemistry, Sun Yat-sen University, Guangzhou 510275, China

† Electronic supplementary information (ESI) available: Experimental details; auxiliary analysis. See DOI: 10.1039/c8ta00587g

we have successfully prepared Si nanorods (SNRs) from natural sepiolite by a simple self-templating synthesis method, which could be very promising in scalable production due to the abundant and low-cost precursor and facile approach. Owing to the intrinsic crystal structure and chemical composition of sepiolite, the 1D structure of SNRs was maintained during magnesiothermic reduction without the addition of templates and heat scavengers. The as-prepared SNRs exhibited a large specific surface area ($\sim$122 m^2 g^{-1}) and hierarchical porous structure (*i.e.*, macro- and mesopores). When used as the anode materials for LIBs, the SNR anodes showed prominent electrochemical performance including excellent rate capability (reversible capacity of 1350 mA h g^{-1} at 1.0 A g^{-1} and 478 mA h g^{-1} at 10 A g^{-1}), remarkable cycling stability (capacity retention of 98% at 5.0 A g^{-1} after 500 cycles), and low volume expansion ($\sim$50%) of electrodes after 100 cycles at 1.0 A g^{-1}.

Experimental

Materials

Pristine sepiolite (Hebei, China) was first purified by a simple sedimentation method, dried overnight, and then collected (purity >98%) for the following experiments. Magnesium (Mg) powder was of analytical grade and supplied by Shanghai Aladdin Chemical Reagent Co., Ltd. Hydrochloric acid (HCl, 37 wt%) and hydrofluoric acid (HF, 40 wt%) were purchased from Guangzhou Chemical Reagent Factory, China.

Materials synthesis

SNRs were prepared by the self-templating synthesis method involved in magnesiothermic reduction. According to the known magnesiothermic reduction reaction ($SiO_2(s) + 2Mg(g) \rightarrow Si(s) + 2MgO(s)$), SiO_2 can be completely reduced by Mg in a weight ratio of 1 : 0.8. Considering the calculated chemical formula of sepiolite (*i.e.*, $Mg_8Si_{12}O_{30}(OH)_4(OH_2)_4 \cdot 8H_2O$) and the actual mass transfer process, we used the stoichiometric weight ratio of sepiolite/Mg as 1 : 0.6. In a typically procedure, sepiolite (1 g) and Mg powder (0.6 g) were fine mixed in a mass ration of 1 : 0.6 and then sealed into a stainless steel reactor in an argon-filled glovebox. Subsequently, this reactor was placed in the middle of a tube furnace and heated to 650 °C at a rate of 5° min^{-1} and held for 5 h under a constant argon flow. After cooling down to room temperature, the resultant mixtures were washed with 100 mL 1 mol L^{-1} HCl for 5 h to remove the byproducts (*e.g.*, MgO), followed by leaching with 100 mL 1% HF. Finally, the resulting silicon products, SNRs, were collected after rinsing thoroughly with distilled water and vacuum-drying overnight.

Characterization

The scanning electron microscopy (SEM) images and energy dispersive X-ray spectroscopy (EDS) results were obtained by using an SU-8010 cold field emission scanning electron microscope (Hitachi, Japan). Transmission electron microscopy (TEM) images and high-resolution TEM (HRTEM) images were recorded on an FEI Talos F200S field-emission transmission electron microscope (FEI Co., USA) with selected area electron diffraction (SAED) attachments at an acceleration voltage of 200 kV. The X-ray diffraction (XRD) patterns of the samples at different stages were obtained on a Bruker D8 ADVANCE X-ray diffractometer (Bruker AXS, Germany), operating at 40 kV and 40 mA with Ni-filtered CuKα radiation ($\lambda = 0.154$ nm). Raman spectra were performed on a Renishaw 2000 confocal micro-Raman Spectrometer (Renishaw, UK) with an air-cooled CCD detector and an Ar-ion laser ($\lambda = 514.5$ nm). The high resolution Si 2p X-ray photoelectron spectroscopy (XPS) spectrum was recorded on a Thermo Fisher K-Alpha XPS instrument (Thermo Fisher Scientific, UK) with a monochromatic Al-Kα X-ray source (1468.6 eV). N_2 adsorption–desorption isotherm of SNRs was collected at liquid nitrogen temperature (−196 °C) on an ASAP 2020 system (Micromeritics, USA). Before measurement, SNRs were outgassed at 200 °C for 12 h under vacuum. The specific surface area was evaluated by using the multi-point Brunauer–Emmett–Teller (BET) equation and the total pore volume was obtained from N_2 adsorption capacity at a relative pressure of 0.97. The pore size distribution was calculated based on the Barrett–Joyner–Halenda (BJH) method.

Electrochemical measurements

The electrochemical performance of the as-prepared SNRs was investigated in a coin-type half-cell (CR2032) which was assembled in an argon-filled glovebox (less than 0.1 ppm of both H_2O and O_2). The working electrode was prepared as follows: the resulting SNRs, acetylene black (Super P), and sodium alginate (SA, analytical grade) binder were homogeneously mixed at a mass ratio of 6 : 2 : 2 in distilled water; then, the slurry was blade-coated on a copper foil and vacuum-dried at 60 °C for 12 h. The mass loading of SNRs was around 0.7 mg cm^{-2}. For coin-cell fabrication, the cast electrodes were cut into disks as working electrodes. Lithium foils were employed as the counter and reference electrodes and polyethylene membranes (Celgard 2400) as separators. The electrolyte consisted of 1 M $LiPF_6$ solution in ethylene carbonate/dimethyl carbonate (EC/DMC, 1 : 1 v/v) and 10 wt% fluorinated ethylene carbonate additives. The rate performance and cycling stability were evaluated at room temperature on a CT2001A multichannel Battery Test System in a voltage window between 0.001 and 1.5 V (*vs.* Li/Li^+). Cyclic voltammetry (CV) measurements were performed on a CHI660D electrochemical workstation with a scan rate of 0.1 mV s^{-1} in the voltage range of 0.001–1.5 V (*vs.* Li/Li^+). The specific capacity in this study was evaluated based on the mass of active materials only. Electrochemical impedance spectroscopy was carried out with an alternating current perturbation of 5 mV in the frequency range from 0.01 to 100 kHz. After the electrochemical test, the cells were disassembled in an argon-filled glovebox, and the working electrodes were completely rinsed with dimethyl carbonate and dried for further characterization.

Results and discussion

The schematic illustration demonstrates the synthetic process of SNRs from natural sepiolite (Fig. 1a). Sepiolite is a typical

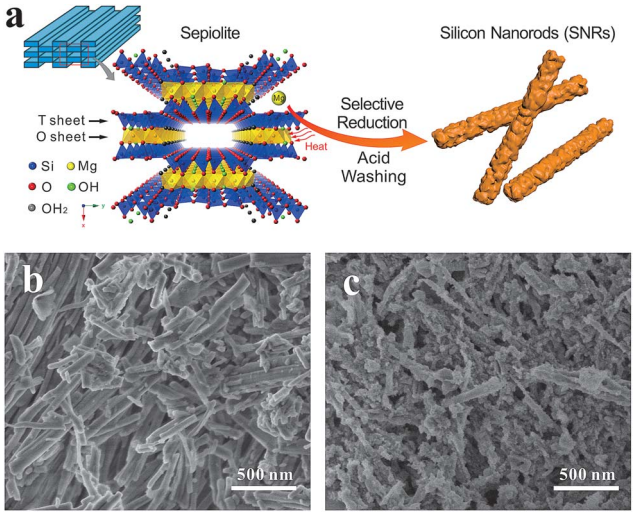

Fig. 1 (a) Schematic illustration of the synthesis of SNRs from natural sepiolite. (b) SEM image of natural sepiolite showing a 1D nanofiber morphology. (c) SEM image of 1D SNRs.

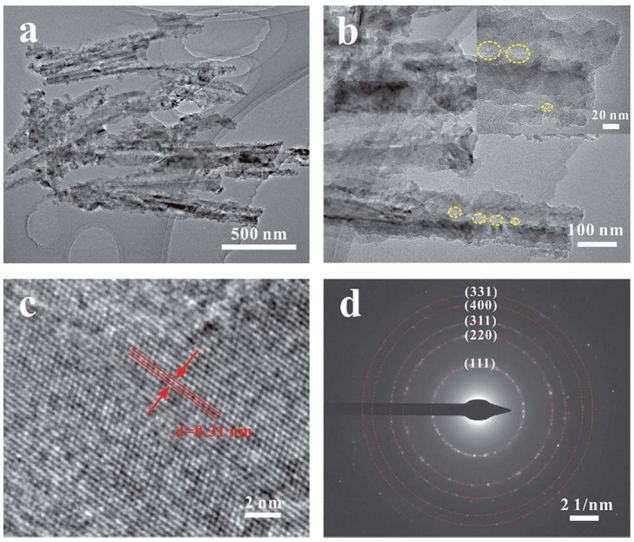

Fig. 2 Morphological characterization of SNRs. (a and b) TEM images (the yellow circles represent the mesopores in the nanorods), (c) HRTEM image showing the crystalline structure, and (d) the corresponding SAED pattern.

2 : 1 type clay mineral with one octahedral (O) sheet sandwiched between two tetrahedral (T) sheets. Unlike ideal phyllosilicates,[36,37] sepiolite possesses a discontinuous O sheet due to the periodic inversion of apical oxygen atoms of the tetrahedron, forming a fibrous pattern with nanosized channels (0.37 × 1.06 nm) running parallel to the fiber.[38] The reduction reaction between Mg and the external silicon–oxygen T sheets was initiated over 550 °C.[17] When the temperature reached the fusion point of Mg (648 °C), Mg atoms readily enter the nanosized channels of sepiolite and attack T sheets inside. The X-ray diffraction (XRD) pattern of intermediates after magnesiothermic reduction showed the presence of the characteristic reflections of Si and MgO but the disappearance of those of raw sepiolite (Fig. S1a, b, ESI†), which suggested a complete reduction of sepiolite. A small amount of Mg_2Si was simultaneously formed in the local Mg-rich surroundings. Subsequently, selective acid treatment was employed to remove all of the byproducts and achieve the final product SNRs. The XRD pattern of SNRs manifested the formation of a well-crystallized silicon phase (Fig. S1c, ESI†).

The SEM images of SNRs showed that the resulting Si product exhibited a morphology of nanorods with a rough surface, almost maintaining the original 1D nanostructure of sepiolite (Fig. 1b, c). The corresponding EDS result confirmed the high purity of SNRs after acid treatment (Fig. S2, ESI†). The TEM images of SNRs further disclosed that the fibrous texture was composed of interconnected or overlapped Si nanoparticles (Fig. 2a, b). Moreover, hierarchical porous architectures were observed, *i.e.*, macropores built by the stacking or aggregation of nanorods and mesopores in the nanorods (marked by the yellow circles). The measured interplanar spacing was ~0.31 nm in the HRTEM image, corresponding to the (111) plane of crystalline Si (Fig. 2c). The SAED pattern further verified the high crystallinity of SNRs due to the distinct diffraction rings that can be indexed to Si (Fig. 2d), consistent with the XRD result. In addition, the EDS mapping and spectra of TEM images strongly demonstrated the high purity of the as-prepared SNRs (Fig. S3, ESI†).

As reported by previous studies, massive heat generated from magnesiothermic reduction reaction would heavily destroy the structures of Si precursors and even fuse the resultant Si nanoparticles into bulk crystals.[39] Therefore, several studies introduced a molten inorganic salt as a heat absorbent to scavenge the excessive heat.[39,40] Interestingly, SNRs in our work still kept a similar nanorod structure to sepiolite without the addition of a heat scavenger. The successful self-templating synthesis of SNRs might be primarily attributed to three reasons: (1) the magnesium–oxygen/hydroxide O sheet (*i.e.*, brucite-like sheet) could absorb the heat *via* its decomposition ($Mg(OH)_2(s) \rightarrow MgO(s) + H_2O(g)$; $\Delta H = 1.4$ kJ $g_{Mg(OH)_2}^{-1}$);[41] (2) the intact trioctahedral sheets (Fig. S4a, ESI†) acted as isolation barriers to inhibit the random bonding of newly formed Si nanoparticles during the reaction, effectively keeping the nanostructure of original sepiolite; and (3) the O sheet-converted MgO with high specific heat capacity was located within two T sheets, which then could serve as a negative catalyst to slow down the exothermic reaction.[42]

To further verify the important role of O sheets in forming SNRs, a control experiment using fibrous palygorskite (Fig. S5a, b†) as a Si precursor was conducted under the same preparation conditions. Compared with sepiolite, palygorskite has a similar chain-layered structure but a different composition (*i.e.*, a large amount of Al exists in O sheets due to massive isomorphous substitution of Mg^{2+} by Al^{3+}) (Fig. S4b, ESI†). Noticeably, a severely agglomerated morphology was visible in the SEM image of the final Si products (Fig. S5c, ESI†). Besides, a small amount of high-temperature phase (*i.e.*, spinel and forsterite) appeared simultaneously in the corresponding XRD pattern (Fig. S5d, ESI†). These results indicated a higher reaction temperature in the palygorskite system than that in the

sepiolite system, which could be ascribed to the lower endothermic capacity of the decomposition of aluminium–oxygen/hydroxide O sheets (ΔH = 1.0 kJ $g_{Al(OH)_3}^{-1}$). Furthermore, different from the true trioctahedral sepiolite, palygorskite is an intermediate between di and trioctahedral clay minerals.[38] The vacant octahedral sites usually emerge at the edge of the ribbons in the Mg-deficient parts (Fig. S4b, ESI†), which allows Mg atoms to attack the aluminium–oxygen/hydroxide O sheets. As a result, the O sheet of palygorskite could not function as an effective template to maintain the original structure.

The resulting SNRs from sepiolite were further analyzed by Raman spectroscopy (Fig. 3a). Compared with the sharp Raman band at ~521 cm^{-1} (resulting from the Si–Si stretching mode) of monocrystalline Si (Fig. S6, ESI†), that of SNRs red-shifted to ~513 cm^{-1} and widened. Besides, two broad peaks at 301 and 938 cm^{-1}, corresponding to the overtones of TA(X) and TO(L), respectively,[43] exhibited the same trends. Similar phenomena were reported in other studies about Si nanostructures,[39,44] which was attributed to the decreased diameters of Si. The high resolution Si 2p XPS spectrum of SNRs showed an intense asymmetric peak mainly composed of Si $2p_{1/2}$ and Si $2p_{3/2}$ of pure Si at ~99.9 and ~99.3 eV (Fig. 3b),[18] respectively. The three very weak peaks at ~100.5, ~101.4, and ~103.0 eV, assigned to SiO_x derivatives, suggested the presence of an almost negligible amount of amorphous SiO_x on the surface of SNRs, which probably originated from the post-oxidation of Si nanocrystals in air.[44]

The pore structure of SNRs was investigated *via* the N_2 adsorption–desorption isotherm (Fig. 3c, d). The obtained isotherm of SNRs belongs to characteristic type IV, with a type H3 hysteresis loop indicative of non-rigid slit-like pores. The rapid increase of N_2 adsorption capacity in the high relative pressure range indicated the existence of macropores, in good agreement with the TEM observation. Moreover, SNRs showed a broad distribution of pore size from 2 to 100 nm, with the most probable pore size at ~32 nm, according to the pore size distribution plot evaluated by the BJH method. The calculated specific surface area of SNRs based on the multi-point BET equation was 122 $m^2 g^{-1}$, and the total pore volume was 0.43 $cm^3 g^{-1}$.

To evaluate the electrochemical performance of SNRs as anodes for LIBs, CR2032 coin-type half cells were assembled in an argon-filled glovebox. The CV plots of the SNR anode were obtained at a scan rate of 0.1 mV s^{-1} (Fig. 4a). A broad and weak peak at ~1.19 V occurred in the first discharge scan and then disappeared from the second cycle onwards, suggesting the formation of a stable solid electrolyte interphase (SEI) film on the surface of SNRs due to the decomposition of the electrolyte.[13] The reductive peaks (0.1 and 0.17 V) assigned to the lithiation process and oxidative peaks (0.36 and 0.51 V) resulting from the delithiation process gradually increased in intensity and then coincided.[45] The phenomenon indicated a kinetic enhancement process of the SNR electrode before stabilization, which usually occurs for Si-based anodes.[30,46,47]

As shown by the galvanostatic discharge–charge curves of the SNR anode (Fig. 4b), a long and flat voltage plateau emerged at ~0.1 V in the first discharge curve, suggesting the alloying reaction between lithium and crystalline Si.[48] The SNR anode exhibited a first discharge/charge capacity of 2705/1635 mA h g^{-1}

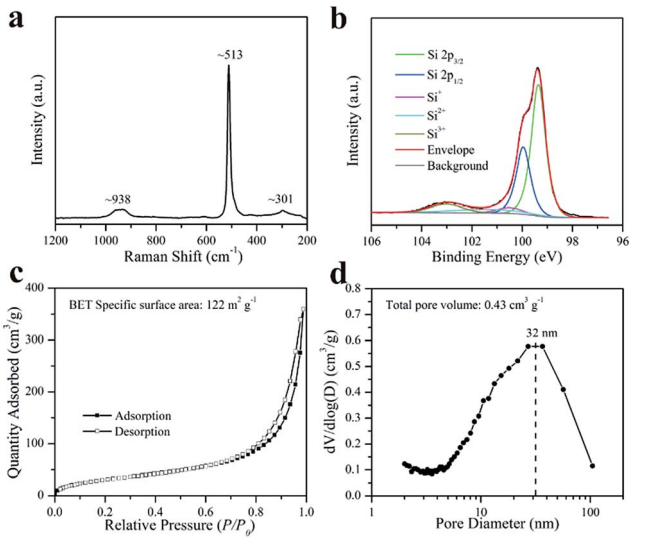

Fig. 3 Characterization of SNRs. (a) Raman spectrum, (b) high resolution Si 2p XPS spectrum, (c) N_2 adsorption–desorption isotherm, and (d) the corresponding BJH pore size distribution curve.

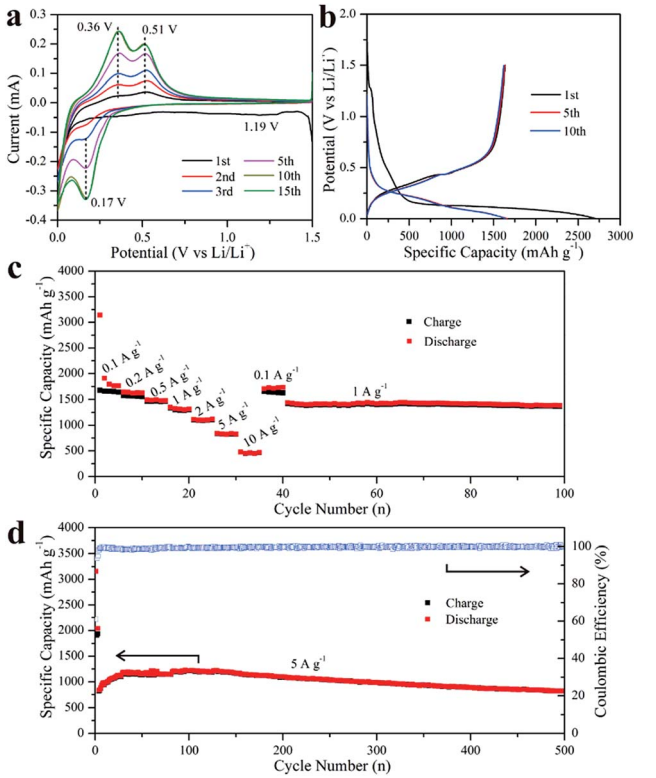

Fig. 4 Electrochemical performances of the SNR anodes. (a) CV curves at a scan rate of 0.1 mV s^{-1} in the voltage range of 0.001–1.5 V (*vs.* Li/Li^+); (b) discharge–charge curves at a current density of 0.2 A g^{-1} between 0.001 and 1.5 V (*vs.* Li/Li^+); (c) rate capability at various current densities from 0.1 to 10 A g^{-1}; (d) cycling performance at a current density of 0.2 A g^{-1} for the initial three cycles and 5.0 A g^{-1} for the remaining cycles.

with an initial coulombic efficiency (CE) of 60.5%. The moderate initial CE was probably associated with the large specific surface area of SNRs which could facilitate the generation of a SEI film.[48,49] Noticeably, this disadvantage could be overcome by simple prelithiation (Fig. S7, ESI†).[40,50] In the subsequent cycle, the voltage plateau was replaced by sloping curves, owing to the formed amorphous phase during the first lithiation/delithiation process.[46] Despite the capacity loss in the first cycle, the SNR anode rapidly reached a high CE over 98% after several cycles. Moreover, the discharge–charge curves for the 5th and 10th cycles were almost overlapped, indicating a superior reversible electrochemical process between the SNR electrode and lithium ions. Noticeably, it took 10 cycles to reach a steady state in the discharge–charge curves, while 15 cycles in CV curves (Fig. 4a and b), which may be attributed to the different current densities. The current density for the oxidative peak (0.36 V) in the CV tests was calculated to be ~0.4 A g^{-1}, much larger than that in the discharge–charge measurements (0.2 A g^{-1}). With the small current density, the electrode had enough time to be activated completely, so the electrode could be stabilized after several cycles.

The SNR electrode displayed the reversible discharge capacities of ~1794, 1644, 1494, 1350, 1116, 841, and 478 mA h g^{-1} at 0.1, 0.2, 0.5, 1.0, 2.0, 5.0, and 10 A g^{-1} (Fig. 4c), respectively. The specific capacity was restored to the initial value when the current density was back to 0.1 A g^{-1}, manifesting the efficient kinetics for lithium storage. Remarkably, as the current density was abruptly switched to 1.0 A g^{-1}, the SNR electrode delivered a quite stable capacity of ~1400 mA h g^{-1}, indicating a good cycling stability. The long-term cycling stability of the SNR electrode at high current density was also evaluated (Fig. 4d). A high capacity of ~816 mA h g^{-1} was still retained after 500 cycles at a high current density of 5.0 A g^{-1}, corresponding to an outstanding capacity retention of 98%. It is noteworthy that the specific capacity of the SNR electrode slightly increased during the first 30 cycles, consistent with the CV results. Such phenomena were not rare for various nanostructured anodes (*e.g.*, Si and metal oxides),[51–54] which could be ascribed to the gradual activation of active materials at high current density, the enhanced electrolyte wetting during cycling, and the generation/dissolution of an organic gel-like coating on the surface of the electrode.[51–54] Besides, the electrochemical impedance spectroscopy spectra further disclosed that the SNR electrode after 100 cycles possessed lower charge transfer resistance and ionic diffusion resistance than the electrode after 3 cycles, as verified by the decreased diameter of the high-frequency semicircle and the increased slope of the low-frequency line (Fig. 5).[55] These results were further confirmed by the fitted data based on the equivalent circuit (Fig. S8, ESI†). In addition, the SNR electrode showed a high CE close to 100% during cycling after the first several cycles. Remarkably, the SNR electrodes still exhibited good cycling performance with a higher active mass loading (~1.1 mg cm^{-2}) or a different ratio of active material, binder, and conductive agent (7 : 1.5 : 1.5) (Fig. S9, ESI†).

The volume expansion of the SNR electrode during the repeated lithium insertion/extraction was further investigated

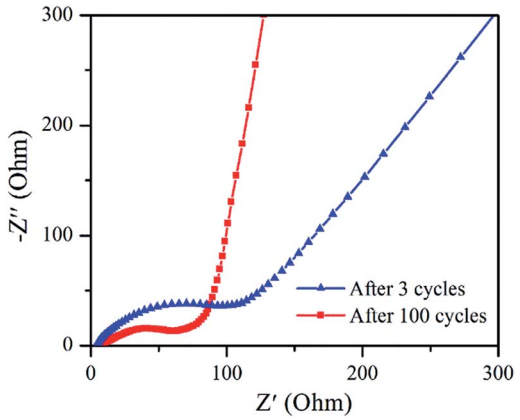

Fig. 5 Nyquist plots of the SNR electrodes after 3 and 100 cycles at 5.0 A g^{-1}.

by obtaining the cross-sectional SEM images of electrodes before and after 100 cycles at 1.0 A g^{-1} (Fig. S10, ESI†). The SNR electrode exhibited an obviously suppressed volume expansion (~50%), compared to conventional bulk Si (>300%), reflecting the good interfacial stability of the SNR electrode during cycling. The superior electrochemical performance of the SNR electrode may result from the following several reasons: (1) the SNRs with a hierarchical porous structure could effectively accommodate interior stress upon the uptake of lithium ions, causing a reduced volume expansion; (2) the 1D structure composed of interconnected Si nanoparticles contributed to shortening the diffusion path of lithium ions and facilitating the charge transport, which enabled the SNR anode to endure high current density; (3) the relatively rough surface of SNRs increased the surface area and electrochemical reaction sites, which was beneficial to the lithium insertion and extraction.[11,56] Without sophisticated designs and surface modification, the SNR anode in our work showed excellent rate performance and cycling stabilization from a practical point of view, in comparison with recently reported 1D Si-based anodes synthesized through other methods (Table S1, ESI†).

Conclusions

In summary, 1D silicon nanorods with a hierarchical porous structure were successfully synthesized from natural sepiolite by a simple self-templating synthesis method. Without complex pre/post-treatment and extra additives (*e.g.*, templates or heat scavengers), the 1D structure of SNRs was maintained during magnesiothermic reduction, owing to the intrinsic crystal structure and chemical composition of sepiolite. As an anode material for LIBs, SNRs exhibited outstanding electrochemical performance in terms of excellent rate capability, remarkable cycling stability, and low volume expansion. Our work provided a facile, low-cost, and scalable strategy for synthesizing 1D nanostructured Si from natural clay minerals, which would be very promising in the practical production and application of high-performance anode materials in LIBs.

Conflicts of interest

There are no conflicts to declare.

Acknowledgements

This work was financially supported by the National Natural Science Foundation of China (41572031), the National Program for Support of Top-notch Young Professionals, and the Guangdong Provincial Program for Support of Top-notch Young Professionals (2014TQ01Z249). This is contribution No. IS-2514 from GIGCAS.

Notes and references

1 B. Dunn, H. Kamath and J.-M. Tarascon, *Science*, 2011, **334**, 928–935.
2 L. Croguennec and M. R. Palacin, *J. Am. Chem. Soc.*, 2015, **137**, 3140–3156.
3 J. Luo, J. Gao, A. Wang and J. Huang, *ACS Nano*, 2015, **9**, 9432–9436.
4 D. Andre, H. Hain, P. Lamp, F. Maglia and B. Stiaszny, *J. Mater. Chem. A*, 2017, **5**, 17174–17198.
5 N.-S. Choi, Z. Chen, S. A. Freunberger, X. Ji, Y.-K. Sun, K. Amine, G. Yushin, L. F. Nazar, J. Cho and P. G. Bruce, *Angew. Chem., Int. Ed.*, 2012, **51**, 9994–10024.
6 S. Goriparti, E. Miele, F. De Angelis, E. Di Fabrizio, R. P. Zaccaria and C. Capiglia, *J. Power Sources*, 2014, **257**, 421–443.
7 W. Qi, J. G. Shapter, Q. Wu, T. Yin, G. Gao and D. Cui, *J. Mater. Chem. A*, 2017, **5**, 19521–19540.
8 H. Wu and Y. Cui, *Nano Today*, 2012, **7**, 414–429.
9 N. Liu, Z. Lu, J. Zhao, M. T. McDowell, H.-W. Lee, W. Zhao and Y. Cui, *Nat. Nanotechnol.*, 2014, **9**, 187–192.
10 L. Lin, X. Xu, C. Chu, M. K. Majeed and J. Yang, *Angew. Chem., Int. Ed.*, 2016, **55**, 14063–14066.
11 X. Zuo, J. Zhu, P. Müller-Buschbaum and Y.-J. Cheng, *Nano Energy*, 2017, **31**, 113–143.
12 J. K. Lee, C. Oh, N. Kim, J.-Y. Hwang and Y.-K. Sun, *J. Mater. Chem. A*, 2016, **4**, 5366–5384.
13 X. Zhou, Y.-X. Yin, L.-J. Wan and Y.-G. Guo, *Chem. Commun.*, 2012, **48**, 2198–2200.
14 X. Tang, G. Wen, Y. Zhang, D. Wang and Y. Song, *Appl. Surf. Sci.*, 2017, **425**, 742–749.
15 Y. F. Dong, T. Slade, M. J. Stolt, L. S. Li, S. N. Girard, L. Q. Mai and S. Jin, *Angew. Chem., Int. Ed.*, 2017, **56**, 14453–14457.
16 C. Hwang, K. Lee, H. D. Um, Y. D. Lee, K. Seo and H. K. Song, *J. Electrochem. Soc.*, 2017, **164**, A1564–A1568.
17 W.-S. Kim, Y. Hwa, J.-H. Shin, M. Yang, H.-J. Sohn and S.-H. Hong, *Nanoscale*, 2014, **6**, 4297–4302.
18 K. Adpakpang, S. B. Patil, S. M. Oh, J.-H. Kang, M. Lacroix and S.-J. Hwang, *Electrochim. Acta*, 2016, **204**, 60–68.
19 P. Gao, H. Tang, A. Xing and Z. Bao, *Electrochim. Acta*, 2017, **228**, 545–552.
20 Y. Zhang, N. Du, S. Zhu, Y. Chen, Y. Lin, S. Wu and D. Yang, *Electrochim. Acta*, 2017, **252**, 438–445.
21 K.-Q. Peng, X. Wang, L. Li, Y. Hu and S.-T. Lee, *Nano Today*, 2013, **8**, 75–97.
22 Y. Zhou, X. Jiang, L. Chen, J. Yue, H. Xu, J. Yang and Y. Qian, *Electrochim. Acta*, 2014, **127**, 252–258.
23 K. Q. Peng, J. J. Hu, Y. J. Yan, Y. Wu, H. Fang, Y. Xu, S. T. Lee and J. Zhu, *Adv. Funct. Mater.*, 2006, **16**, 387–394.
24 A. Vlad, A. L. M. Reddy, A. Ajayan, N. Singh, J.-F. Gohy, S. Melinte and P. M. Ajayan, *Proc. Natl. Acad. Sci. U. S. A.*, 2012, **109**, 15168–15173.
25 M. Y. Ge, J. P. Rong, X. Fang and C. W. Zhou, *Nano Lett.*, 2012, **12**, 2318–2323.
26 X. Han, H. Chen, X. Li, J. Wang, C. Li, S. Chen and Y. Yang, *J. Mater. Chem. A*, 2016, **4**, 434–442.
27 C. K. Chan, H. Peng, G. Liu, K. McIlwrath, X. F. Zhang, R. A. Huggins and Y. Cui, *Nat. Nanotechnol.*, 2008, **3**, 31–35.
28 X. Huang, J. Yang, S. Mao, J. Chang, P. B. Hallac, C. R. Fell, B. Metz, J. Jiang, P. T. Hurley and J. Chen, *Adv. Mater.*, 2014, **26**, 4326–4332.
29 R. Epur, P. J. Hanumantha, M. K. Datta, D. Hong, B. Gattu and P. N. Kumta, *J. Mater. Chem. A*, 2015, **3**, 11117–11129.
30 Y. Jiang, Y. Zhang, X. Yan, M. Tian, W. Xiao and H. Tang, *Chem. Eng. J.*, 2017, **330**, 1052–1059.
31 J.-K. Yoo, J. Kim, Y. S. Jung and K. Kang, *Adv. Mater.*, 2012, **24**, 5452–5456.
32 D. J. Lee, H. Lee, M.-H. Ryou, G.-B. Han, J.-N. Lee, J. Song, J. Choi, K. Y. Cho, Y. M. Lee and J.-K. Park, *ACS Appl. Mater. Interfaces*, 2013, **5**, 12005–12010.
33 V. Cecen, A. Boudenne, L. Ibos, I. Novak, Z. Nogellova, J. Prokes and I. Krupa, *Eur. Polym. J.*, 2008, **44**, 3827–3834.
34 P. Aranda, R. Kun, M. A. Martin-Luengo, S. Letaief, I. Dekany and E. Ruiz-Hitzky, *Chem. Mater.*, 2008, **20**, 84–91.
35 F. Bergaya and G. Lagaly, in *Developments in Clay Science*, ed. F. Bergaya, B. K. G. Theng and G. Lagaly, Elsevier, 2006, vol. 1, pp. 1–18.
36 Q. Chen, R. Zhu, L. Ma, Q. Zhou, J. Zhu and H. He, *Appl. Clay Sci.*, 2017, **135**, 129–135.
37 R. Zhu, Q. Chen, Q. Zhou, Y. Xi, J. Zhu and H. He, *Appl. Clay Sci.*, 2016, **123**, 239–258.
38 M. Brigatti, E. Galan and B. Theng, *Dev. Clay Sci.*, 2006, **1**, 19–86.
39 W. Luo, X. Wang, C. Meyers, N. Wannenmacher, W. Sirisaksoontorn, M. M. Lerner and X. Ji, *Sci. Rep.*, 2013, **3**.
40 J. Ryu, D. Hong, S. Choi and S. Park, *ACS Nano*, 2016, **10**, 2843–2851.
41 J. G. Speight, *Lange's handbook of chemistry*, McGraw-Hill, New York, 2005.
42 K. Nishiyama, T. Ono, A. Nakayama, H. Sakai, M. Koishi and M. Abe, *Surf. Coat. Int. B: Coat. Trans.*, 2003, **86**, 169–174.
43 R. P. Wang, G. W. Zhou, Y. L. Liu, S. H. Pan, H. Z. Zhang, D. P. Yu and Z. Zhang, *Phys. Rev. B*, 2000, **61**, 16827–16832.
44 Y. Han, N. Lin, Y. Qian, J. Zhou, J. Tian, Y. Zhu and Y. Qian, *Chem. Commun.*, 2016, **52**, 3813–3816.
45 T. Jaumann, M. Gerwig, J. Balach, S. Oswald, E. Brendler, R. Hauser, B. Kieback, J. Eckert, L. Giebeler and E. Kroke, *J. Mater. Chem. A*, 2017, **5**, 9262–9271.
46 J. Zhu, J. Yang, Z. Xu, J. Wang, Y. Nuli, X. Zhuang and X. Feng, *Nanoscale*, 2017, **9**, 8871–8878.

47 Y. H. Huang, Q. Bao, J. G. Duh and C. T. Chang, *J. Mater. Chem. A*, 2016, **4**, 9986–9997.
48 X. Zuo, Y. Xia, Q. Ji, X. Gao, S. Yin, M. Wang, X. Wang, B. Qiu, A. Wei, Z. Sun, Z. Liu, J. Zhu and Y.-J. Cheng, *ACS Nano*, 2017, **11**, 889–899.
49 W.-J. Zhang, *J. Power Sources*, 2011, **196**, 13–24.
50 N. A. Liu, L. B. Hu, M. T. McDowell, A. Jackson and Y. Cui, *ACS Nano*, 2011, **5**, 6487–6493.
51 J. Liu, P. Kopold, P. A. van Aken, J. Maier and Y. Yu, *Angew. Chem., Int. Ed.*, 2015, **54**, 9632–9636.
52 N. Lin, L. Wang, J. Zhou, J. Zhou, Y. Han, Y. Zhu, Y. Qian and C. Cao, *J. Mater. Chem. A*, 2015, **3**, 11199–11202.
53 S. Liu, Y. Dong, C. Zhao, Z. Zhao, C. Yu, Z. Wang and J. Qiu, *Nano Energy*, 2015, **12**, 578–587.
54 L. Wu, J. Yang, X. Zhou, M. Zhang, Y. Ren and Y. Nie, *J. Mater. Chem. A*, 2016, **4**, 11381–11387.
55 Q. Yun, X. Qin, W. Lv, Y.-B. He, B. Li, F. Kang and Q.-H. Yang, *Carbon*, 2015, **93**, 59–67.
56 Y. Yao, N. Liu, M. T. McDowell, M. Pasta and Y. Cui, *Energy Environ. Sci.*, 2012, **5**, 7927–7930.